

Measurement of the photon+ b -jet production differential cross section in $p\bar{p}$ collisions at $\sqrt{s} = 1.96$ TeV

V.M. Abazov,³² B. Abbott,⁷¹ B.S. Acharya,²⁶ M. Adams,⁴⁷ T. Adams,⁴⁵ G.D. Alexeev,³² G. Alkhalaf,³⁶ A. Alton^a,⁵⁹ G. Alverson,⁵⁸ M. Aoki,⁴⁶ A. Askew,⁴⁵ S. Atkins,⁵⁶ K. Augsten,⁷ C. Avila,⁵ F. Badaud,¹⁰ L. Bagby,⁴⁶ B. Baldin,⁴⁶ D.V. Bandurin,⁴⁵ S. Banerjee,²⁶ E. Barberis,⁵⁸ P. Baringer,⁵⁴ J. Barreto,² J.F. Bartlett,⁴⁶ N. Bartosik,³⁹ U. Bassler,¹⁵ V. Bazterra,⁴⁷ A. Bean,⁵⁴ M. Begalli,² L. Bellantoni,⁴⁶ S.B. Beri,²⁴ G. Bernardi,¹⁴ R. Bernhard,¹⁹ I. Bertram,⁴⁰ M. Besançon,¹⁵ R. Beuselinck,⁴¹ V.A. Bezzubov,³⁵ P.C. Bhat,⁴⁶ S. Bhatia,⁶¹ V. Bhatnagar,²⁴ G. Blazey,⁴⁸ S. Blessing,⁴⁵ K. Bloom,⁶² A. Boehnlein,⁴⁶ D. Boline,⁶⁸ E.E. Boos,³⁴ G. Borissov,⁴⁰ T. Bose,⁵⁷ A. Brandt,⁷⁴ O. Brandt,²⁰ R. Brock,⁶⁰ G. Brooijmans,⁶⁶ A. Bross,⁴⁶ D. Brown,¹⁴ J. Brown,¹⁴ X.B. Bu,⁴⁶ M. Buehler,⁴⁶ V. Buescher,²¹ V. Bunichev,³⁴ S. Burdin^b,⁴⁰ C.P. Buszello,³⁸ E. Camacho-Pérez,²⁹ B.C.K. Casey,⁴⁶ H. Castilla-Valdez,²⁹ S. Caughron,⁶⁰ S. Chakrabarti,⁶⁸ D. Chakraborty,⁴⁸ K.M. Chan,⁵² A. Chandra,⁷⁶ E. Chapon,¹⁵ G. Chen,⁵⁴ S. Chevalier-Théry,¹⁵ D.K. Cho,⁷³ S.W. Cho,²⁸ S. Choi,²⁸ B. Choudhary,²⁵ S. Cihangir,⁴⁶ D. Claes,⁶² J. Clutter,⁵⁴ M. Cooke,⁴⁶ W.E. Cooper,⁴⁶ M. Corcoran,⁷⁶ F. Couderc,¹⁵ M.-C. Cousinou,¹² A. Croc,¹⁵ D. Cutts,⁷³ A. Das,⁴³ G. Davies,⁴¹ S.J. de Jong,^{30,31} E. De La Cruz-Burelo,²⁹ F. Déliot,¹⁵ R. Demina,⁶⁷ D. Denisov,⁴⁶ S.P. Denisov,³⁵ S. Desai,⁴⁶ C. Deterre,¹⁵ K. DeVaughan,⁶² H.T. Diehl,⁴⁶ M. Diesburg,⁴⁶ P.F. Ding,⁴² A. Dominguez,⁶² A. Dubey,²⁵ L.V. Dudko,³⁴ D. Duggan,⁶³ A. Duperrin,¹² S. Dutt,²⁴ A. Dyshkant,⁴⁸ M. Eads,⁶² D. Edmunds,⁶⁰ J. Ellison,⁴⁴ V.D. Elvira,⁴⁶ Y. Enari,¹⁴ H. Evans,⁵⁰ A. Evdokimov,⁶⁹ V.N. Evdokimov,³⁵ G. Facini,⁵⁸ L. Feng,⁴⁸ T. Ferbel,⁶⁷ F. Fiedler,²¹ F. Filthaut,^{30,31} W. Fisher,⁶⁰ H.E. Fisk,⁴⁶ M. Fortner,⁴⁸ H. Fox,⁴⁰ S. Fuess,⁴⁶ A. Garcia-Bellido,⁶⁷ J.A. García-González,²⁹ G.A. García-Guerra^c,²⁹ V. Gavrilov,³³ P. Gay,¹⁰ W. Geng,^{12,60} D. Gerbaudo,⁶⁴ C.E. Gerber,⁴⁷ Y. Gershtein,⁶³ G. Ginther,^{46,67} G. Golovanov,³² A. Goussiou,⁷⁸ P.D. Grannis,⁶⁸ S. Greder,¹⁶ H. Greenlee,⁴⁶ G. Grenier,¹⁷ Ph. Gris,¹⁰ J.-F. Grivaz,¹³ A. Grohsjean^d,¹⁵ S. Grünendahl,⁴⁶ M.W. Grünewald,²⁷ T. Guillemin,¹³ G. Gutierrez,⁴⁶ P. Gutierrez,⁷¹ A. Haas^e,⁶⁶ S. Hagopian,⁴⁵ J. Haley,⁵⁸ L. Han,⁴ K. Harder,⁴² A. Harel,⁶⁷ J.M. Hauptman,⁵³ J. Hays,⁴¹ T. Head,⁴² T. Hebbeker,¹⁸ D. Hedin,⁴⁸ H. Hegab,⁷² A.P. Heinson,⁴⁴ U. Heintz,⁷³ C. Hensel,²⁰ I. Heredia-De La Cruz,²⁹ K. Herner,⁵⁹ G. Hesketh^f,⁴² M.D. Hildreth,⁵² R. Hirosky,⁷⁷ T. Hoang,⁴⁵ J.D. Hobbs,⁶⁸ B. Hoeneisen,⁹ M. Hohlfeld,²¹ I. Howley,⁷⁴ Z. Hubacek,^{7,15} V. Hynek,⁷ I. Iashvili,⁶⁵ Y. Ilchenko,⁷⁵ R. Illingworth,⁴⁶ A.S. Ito,⁴⁶ S. Jabeen,⁷³ M. Jaffré,¹³ A. Jayasinghe,⁷¹ R. Jesik,⁴¹ K. Johns,⁴³ E. Johnson,⁶⁰ M. Johnson,⁴⁶ A. Jonckheere,⁴⁶ P. Jonsson,⁴¹ J. Joshi,⁴⁴ A.W. Jung,⁴⁶ A. Juste,³⁷ K. Kaadze,⁵⁵ E. Kajfasz,¹² D. Karmanov,³⁴ P.A. Kasper,⁴⁶ I. Katsanos,⁶² R. Kehoe,⁷⁵ S. Kermiche,¹² N. Khalatyan,⁴⁶ A. Khanov,⁷² A. Kharchilava,⁶⁵ Y.N. Kharzheev,³² I. Kiselevich,³³ J.M. Kohli,²⁴ A.V. Kozelov,³⁵ J. Kraus,⁶¹ S. Kulikov,³⁵ A. Kumar,⁶⁵ A. Kupco,⁸ T. Kurča,¹⁷ V.A. Kuzmin,³⁴ S. Lammers,⁵⁰ G. Landsberg,⁷³ P. Lebrun,¹⁷ H.S. Lee,²⁸ S.W. Lee,⁵³ W.M. Lee,⁴⁶ J. Lellouch,¹⁴ H. Li,¹¹ L. Li,⁴⁴ Q.Z. Li,⁴⁶ J.K. Lim,²⁸ D. Lincoln,⁴⁶ J. Linnemann,⁶⁰ V.V. Lipaev,³⁵ R. Lipton,⁴⁶ H. Liu,⁷⁵ Y. Liu,⁴ A. Lobodenko,³⁶ M. Lokajicek,⁸ R. Lopes de Sa,⁶⁸ H.J. Lubatti,⁷⁸ R. Luna-Garcia^g,²⁹ A.L. Lyon,⁴⁶ A.K.A. Maciel,¹ R. Madar,¹⁵ R. Magaña-Villalba,²⁹ S. Malik,⁶² V.L. Malyshev,³² Y. Maravin,⁵⁵ J. Martínez-Ortega,²⁹ R. McCarthy,⁶⁸ C.L. McGivern,⁵⁴ M.M. Meijer,^{30,31} A. Melnitchouk,⁶¹ D. Menezes,⁴⁸ P.G. Mercadante,³ M. Merkin,³⁴ A. Meyer,¹⁸ J. Meyer,²⁰ F. Miconi,¹⁶ N.K. Mondal,²⁶ M. Mulhearn,⁷⁷ E. Nagy,¹² M. Naimuddin,²⁵ M. Narain,⁷³ R. Nayyar,⁴³ H.A. Neal,⁵⁹ J.P. Negret,⁵ P. Neustroev,³⁶ T. Nunnemann,²² G. Obrant[‡],³⁶ J. Orduna,⁷⁶ N. Osman,¹² J. Osta,⁵² M. Padilla,⁴⁴ A. Pal,⁷⁴ N. Parashar,⁵¹ V. Parihar,⁷³ S.K. Park,²⁸ R. Partridge^e,⁷³ N. Parua,⁵⁰ A. Patwa,⁶⁹ B. Penning,⁴⁶ M. Perfilov,³⁴ Y. Peters,⁴² K. Petridis,⁴² G. Petrillo,⁶⁷ P. Pétrouff,¹³ M.-A. Pleier,⁶⁹ P.L.M. Podesta-Lerma^h,²⁹ V.M. Podstavkov,⁴⁶ A.V. Popov,³⁵ M. Prewitt,⁷⁶ D. Price,⁵⁰ N. Prokopenko,³⁵ J. Qian,⁵⁹ A. Quadt,²⁰ B. Quinn,⁶¹ M.S. Rangel,¹ K. Ranjan,²⁵ P.N. Ratoff,⁴⁰ I. Razumov,³⁵ P. Renkel,⁷⁵ I. Ripp-Baudot,¹⁶ F. Rizatdinova,⁷² M. Rominsky,⁴⁶ A. Ross,⁴⁰ C. Royon,¹⁵ P. Rubinov,⁴⁶ R. Ruchti,⁵² G. Sajot,¹¹ P. Salcido,⁴⁸ A. Sánchez-Hernández,²⁹ M.P. Sanders,²² B. Sanghi,⁴⁶ A.S. Santosⁱ,¹ G. Savage,⁴⁶ L. Sawyer,⁵⁶ T. Scanlon,⁴¹ R.D. Schamberger,⁶⁸ Y. Scheglov,³⁶ H. Schellman,⁴⁹ S. Schlobohm,⁷⁸ C. Schwanenberger,⁴² R. Schwienhorst,⁶⁰ J. Sekaric,⁵⁴ H. Severini,⁷¹ E. Shabalina,²⁰ V. Shary,¹⁵ S. Shaw,⁶⁰ A.A. Shchukin,³⁵ R.K. Shivpuri,²⁵ V. Simak,⁷ P. Skubic,⁷¹ P. Slattery,⁶⁷ D. Smirnov,⁵² K.J. Smith,⁶⁵ G.R. Snow,⁶² J. Snow,⁷⁰ S. Snyder,⁶⁹ S. Söldner-Rembold,⁴² L. Sonnenschein,¹⁸ K. Soustruznik,⁶ J. Stark,¹¹ D.A. Stoyanova,³⁵ M. Strauss,⁷¹ L. Stutte,⁴⁶ L. Suter,⁴² P. Svoisky,⁷¹ M. Takahashi,⁴² M. Titov,¹⁵ V.V. Tokmenin,³² Y.-T. Tsai,⁶⁷ K. Tschann-Grimm,⁶⁸ D. Tsybychev,⁶⁸ B. Tuchming,¹⁵ C. Tully,⁶⁴

L. Uvarov,³⁶ S. Uvarov,³⁶ S. Uzunyan,⁴⁸ R. Van Kooten,⁵⁰ W.M. van Leeuwen,³⁰ N. Varelas,⁴⁷ E.W. Varnes,⁴³ I.A. Vasilyev,³⁵ P. Verdier,¹⁷ A.Y. Verkheev,³² L.S. Vertogradov,³² M. Verzocchi,⁴⁶ M. Vesterinen,⁴² D. Vilanova,¹⁵ P. Vokac,⁷ H.D. Wahl,⁴⁵ M.H.L.S. Wang,⁴⁶ J. Warchol,⁵² G. Watts,⁷⁸ M. Wayne,⁵² J. Weichert,²¹ L. Welty-Rieger,⁴⁹ A. White,⁷⁴ D. Wicke,²³ M.R.J. Williams,⁴⁰ G.W. Wilson,⁵⁴ M. Wobisch,⁵⁶ D.R. Wood,⁵⁸ T.R. Wyatt,⁴² Y. Xie,⁴⁶ R. Yamada,⁴⁶ W.-C. Yang,⁴² T. Yasuda,⁴⁶ Y.A. Yatsunenko,³² W. Ye,⁶⁸ Z. Ye,⁴⁶ H. Yin,⁴⁶ K. Yip,⁶⁹ S.W. Youn,⁴⁶ J. Zennamo,⁶⁵ T. Zhao,⁷⁸ T.G. Zhao,⁴² B. Zhou,⁵⁹ J. Zhu,⁵⁹ M. Zielinski,⁶⁷ D. Zieminska,⁵⁰ and L. Zivkovic⁷³

(The D0 Collaboration*)

¹LAFEX, Centro Brasileiro de Pesquisas Físicas, Rio de Janeiro, Brazil

²Universidade do Estado do Rio de Janeiro, Rio de Janeiro, Brazil

³Universidade Federal do ABC, Santo André, Brazil

⁴University of Science and Technology of China, Hefei, People's Republic of China

⁵Universidad de los Andes, Bogotá, Colombia

⁶Charles University, Faculty of Mathematics and Physics,

Center for Particle Physics, Prague, Czech Republic

⁷Czech Technical University in Prague, Prague, Czech Republic

⁸Center for Particle Physics, Institute of Physics,

Academy of Sciences of the Czech Republic, Prague, Czech Republic

⁹Universidad San Francisco de Quito, Quito, Ecuador

¹⁰LPC, Université Blaise Pascal, CNRS/IN2P3, Clermont, France

¹¹LPSC, Université Joseph Fourier Grenoble 1, CNRS/IN2P3,

Institut National Polytechnique de Grenoble, Grenoble, France

¹²CPPM, Aix-Marseille Université, CNRS/IN2P3, Marseille, France

¹³LAL, Université Paris-Sud, CNRS/IN2P3, Orsay, France

¹⁴LPNHE, Universités Paris VI and VII, CNRS/IN2P3, Paris, France

¹⁵CEA, Irfu, SPP, Saclay, France

¹⁶IPHC, Université de Strasbourg, CNRS/IN2P3, Strasbourg, France

¹⁷IPNL, Université Lyon 1, CNRS/IN2P3, Villeurbanne, France and Université de Lyon, Lyon, France

¹⁸III. Physikalisches Institut A, RWTH Aachen University, Aachen, Germany

¹⁹Physikalisches Institut, Universität Freiburg, Freiburg, Germany

²⁰II. Physikalisches Institut, Georg-August-Universität Göttingen, Göttingen, Germany

²¹Institut für Physik, Universität Mainz, Mainz, Germany

²²Ludwig-Maximilians-Universität München, München, Germany

²³Fachbereich Physik, Bergische Universität Wuppertal, Wuppertal, Germany

²⁴Panjab University, Chandigarh, India

²⁵Delhi University, Delhi, India

²⁶Tata Institute of Fundamental Research, Mumbai, India

²⁷University College Dublin, Dublin, Ireland

²⁸Korea Detector Laboratory, Korea University, Seoul, Korea

²⁹CINVESTAV, Mexico City, Mexico

³⁰Nikhef, Science Park, Amsterdam, the Netherlands

³¹Radboud University Nijmegen, Nijmegen, the Netherlands

³²Joint Institute for Nuclear Research, Dubna, Russia

³³Institute for Theoretical and Experimental Physics, Moscow, Russia

³⁴Moscow State University, Moscow, Russia

³⁵Institute for High Energy Physics, Protvino, Russia

³⁶Petersburg Nuclear Physics Institute, St. Petersburg, Russia

³⁷Institució Catalana de Recerca i Estudis Avançats (ICREA) and Institut de Física d'Altes Energies (IFAE), Barcelona, Spain

³⁸Uppsala University, Uppsala, Sweden

³⁹Taras Shevchenko National University of Kyiv, Kiev, Ukraine

⁴⁰Lancaster University, Lancaster LA1 4YB, United Kingdom

⁴¹Imperial College London, London SW7 2AZ, United Kingdom

⁴²The University of Manchester, Manchester M13 9PL, United Kingdom

⁴³University of Arizona, Tucson, Arizona 85721, USA

⁴⁴University of California Riverside, Riverside, California 92521, USA

⁴⁵Florida State University, Tallahassee, Florida 32306, USA

⁴⁶Fermi National Accelerator Laboratory, Batavia, Illinois 60510, USA

⁴⁷University of Illinois at Chicago, Chicago, Illinois 60607, USA

⁴⁸Northern Illinois University, DeKalb, Illinois 60115, USA

⁴⁹Northwestern University, Evanston, Illinois 60208, USA

⁵⁰Indiana University, Bloomington, Indiana 47405, USA

⁵¹Purdue University Calumet, Hammond, Indiana 46323, USA

⁵²University of Notre Dame, Notre Dame, Indiana 46556, USA

- ⁵³Iowa State University, Ames, Iowa 50011, USA
⁵⁴University of Kansas, Lawrence, Kansas 66045, USA
⁵⁵Kansas State University, Manhattan, Kansas 66506, USA
⁵⁶Louisiana Tech University, Ruston, Louisiana 71272, USA
⁵⁷Boston University, Boston, Massachusetts 02215, USA
⁵⁸Northeastern University, Boston, Massachusetts 02115, USA
⁵⁹University of Michigan, Ann Arbor, Michigan 48109, USA
⁶⁰Michigan State University, East Lansing, Michigan 48824, USA
⁶¹University of Mississippi, University, Mississippi 38677, USA
⁶²University of Nebraska, Lincoln, Nebraska 68588, USA
⁶³Rutgers University, Piscataway, New Jersey 08855, USA
⁶⁴Princeton University, Princeton, New Jersey 08544, USA
⁶⁵State University of New York, Buffalo, New York 14260, USA
⁶⁶Columbia University, New York, New York 10027, USA
⁶⁷University of Rochester, Rochester, New York 14627, USA
⁶⁸State University of New York, Stony Brook, New York 11794, USA
⁶⁹Brookhaven National Laboratory, Upton, New York 11973, USA
⁷⁰Langston University, Langston, Oklahoma 73050, USA
⁷¹University of Oklahoma, Norman, Oklahoma 73019, USA
⁷²Oklahoma State University, Stillwater, Oklahoma 74078, USA
⁷³Brown University, Providence, Rhode Island 02912, USA
⁷⁴University of Texas, Arlington, Texas 76019, USA
⁷⁵Southern Methodist University, Dallas, Texas 75275, USA
⁷⁶Rice University, Houston, Texas 77005, USA
⁷⁷University of Virginia, Charlottesville, Virginia 22901, USA
⁷⁸University of Washington, Seattle, Washington 98195, USA
- (Dated: July 26, 2018)

We present measurements of the differential cross section $d\sigma/dp_T^\gamma$ for the inclusive production of a photon in association with a b -quark jet for photons with rapidities $|y^\gamma| < 1.0$ and $30 < p_T^\gamma < 300$ GeV, as well as for photons with $1.5 < |y^\gamma| < 2.5$ and $30 < p_T^\gamma < 200$ GeV, where p_T^γ is the photon transverse momentum. The b -quark jets are required to have $p_T > 15$ GeV and rapidity $|y^{\text{jet}}| < 1.5$. The results are based on data corresponding to an integrated luminosity of 8.7 fb^{-1} , recorded with the D0 detector at the Fermilab Tevatron $p\bar{p}$ Collider at $\sqrt{s} = 1.96$ TeV. The measured cross sections are compared with next-to-leading order perturbative QCD calculations using different sets of parton distribution functions as well as to predictions based on the k_T -factorization QCD approach, and those from the SHERPA and PYTHIA Monte Carlo event generators.

PACS numbers: 13.85.Qk, 12.38.Bx, 12.38.Qk

In hadron-hadron collisions, high-energy photons (γ) emerge unaltered from the hard scattering process of two partons and therefore provide a clean probe of the parton level dynamics. Study of such photons (called prompt or direct) produced in association with a b -quark also provides information about the b -quark and gluon (g) parton distribution functions (PDFs) of the incoming hadrons. Such events are produced in Quantum Chromodynamics (QCD) primarily through the Compton-like scattering process $gb \rightarrow \gamma b$, which dominates up to photon transverse momenta (p_T^γ) of ≈ 70 GeV, and through quark-antiquark annihilation $q\bar{q} \rightarrow \gamma g \rightarrow \gamma b\bar{b}$, which dominates

at high p_T^γ [1]. The inclusive $\gamma + b$ production may also originate from partonic processes like $gg \rightarrow b\bar{b}$ or $bg \rightarrow bg$, where the final state b -quark or gluon fragments into a photon [1]. However, photon isolation requirements substantially reduce the contributions from this process. The measurements of the differential cross section as a function of p_T^γ and the photon (and/or b -jet) rapidity can be used to test the $\gamma + b$ production mechanism and the underlying dynamics of QCD hard-scattering subprocesses with different momentum transfer scales Q and parton momentum fraction x . Measurements involving γ/Z -boson and b -quark final states have previously been performed by the D0 and CDF collaborations [2–6]. In comparison to the previous $\gamma + b$ measurement [6], we now consider not only the leading (in p_T) b -jet, but all b -jets in the event. To increase statistics in p_T^γ bins, we have also extended the $|y^{\text{jet}}|$ region which results in a larger contribution from the annihilation process. The large integrated luminosity recorded with the D0 detector in $p\bar{p}$ collisions at $\sqrt{s} = 1.96$ TeV at the Fermilab

*with visitors from ^aAugustana College, Sioux Falls, SD, USA, ^bThe University of Liverpool, Liverpool, UK, ^cUPIITA-IPN, Mexico City, Mexico, ^dDESY, Hamburg, Germany, ^eSLAC, Menlo Park, CA, USA, ^fUniversity College London, London, UK, ^gCentro de Investigacion en Computacion - IPN, Mexico City, Mexico, ^hECFM, Universidad Autonoma de Sinaloa, Culiacán, Mexico and ⁱUniversidade Estadual Paulista, São Paulo, Brazil. †Deceased.

Tevatron Collider and more advanced photon and b -jet identification tools [7–9] enable us to perform more precise measurements and to extend them in kinematic regions previously unexplored.

In this Letter, we present measurements of the inclusive $\gamma + b$ -jet production cross sections using data collected from June 2006 to September 2011. The cross sections are measured as a function of p_T^γ in the photon rapidity regions, $|y^\gamma| < 1.0$ (central) and $1.5 < |y^\gamma| < 2.5$ (forward). The rapidity, y , is related to the polar scattering angle θ with respect to the proton beam axis by $y = \frac{1}{2} \ln[(1 + \beta \cos\theta)/(1 - \beta \cos\theta)]$, where β is defined as the ratio between momentum and energy $\beta = |\vec{p}|/E$. The photons are required to have $30 < p_T^\gamma < 300$ GeV in the central rapidity region and $30 < p_T^\gamma < 200$ GeV in the forward region. The b -jets are required to be within $|y^{\text{jet}}| < 1.5$ and to have transverse momentum $p_T^{\text{jet}} > 15$ GeV. This allows us to probe the dynamics of the production process in a wide kinematic range, not studied before in other measurements of a vector boson + b -jet final state. The measurement covers parton momentum fractions in the range $0.007 \lesssim x \lesssim 0.4$. Figure 1 shows the fractional contributions of the $gb \rightarrow \gamma b$ subprocesses to the total cross section of $\gamma + b$ production with photons in the central and forward photon rapidity regions as a function of p_T^γ . The curves are obtained using signal processes $gb \rightarrow \gamma b$ and $q\bar{q} \rightarrow \gamma b\bar{b}$ simulated with the PYTHIA event generator [10]. It can be seen that the Compton-like contribution is large at small p_T^γ and decreases with growing p_T^γ , with the annihilation process contribution having the opposite behavior.

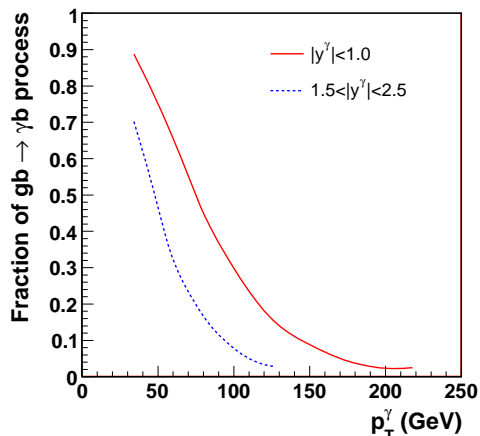


FIG. 1: Fractional contribution of the $gb \rightarrow \gamma b$ subprocess to the associated production of direct photon and b -jet as a function of p_T^γ in the events with photons in the central and forward rapidity regions. The fractions are calculated using PYTHIA 6.4 [10] and the CTEQ6.1L parton distribution functions [11].

The D0 detector is a general purpose detector discussed in detail elsewhere [12]. The subdetectors most

relevant to this analysis are the central tracking system, composed of a silicon microstrip tracker (SMT) and a central fiber tracker (CFT) embedded in a 1.9 T solenoidal magnetic field, the central preshower detector (CPS), and the calorimeter. The CPS is located immediately before the inner layer of the central calorimeter and is formed of approximately one radiation length of lead absorber followed by three layers of scintillating strips. The calorimeter consists of a central section with coverage in pseudorapidity of $|\eta_{\text{det}}| < 1.1$ [13], and two end calorimeters covering up to $|\eta_{\text{det}}| \approx 4.2$. The electromagnetic (EM) section of the calorimeter is segmented longitudinally into four layers (EM i , $i = 1 - 4$), with transverse segmentation into cells of size $\Delta\eta_{\text{det}} \times \Delta\phi_{\text{det}} = 0.1 \times 0.1$ [13], except EM3 (near the EM shower maximum), where it is 0.05×0.05 . The calorimeter allows for a precise measurement of the energy and direction of electrons and photons, providing an energy resolution of approximately 4% (3%) at an energy of 30 (100) GeV, and an angular resolution of 0.01 radians. The energy response of the calorimeter to photons is calibrated using electrons from Z boson decays. Since electrons and photons shower differently in matter, additional energy corrections as a function of y^γ are derived using a detailed GEANT-based [14] simulation of the D0 detector response. These corrections are largest, $\approx 2\%$, at photon energies of about 30 GeV. The data used in this analysis satisfy D0 data quality requirements and are collected using a combination of triggers requiring a cluster of energy in the electromagnetic (EM) calorimeter with loose shower shape requirements, and correspond to an integrated luminosity of $8.7 \pm 0.5 \text{ fb}^{-1}$ [15]. The trigger efficiency is $\approx 96\%$ for photon candidates with $p_T^\gamma \sim 30$ GeV and $\approx 100\%$ for $p_T^\gamma > 40$ GeV.

Offline event selection requires a reconstructed $p\bar{p}$ interaction vertex [16] within 60 cm of the center of the detector along the beam axis. The efficiency of the vertex requirement is $\approx (96 - 98)\%$, depending on p_T^γ . The missing transverse momentum in the event is required to be less than $0.7p_T^\gamma$ to suppress background from $W \rightarrow e\nu$ decays. Such a requirement is highly efficient for signal events, with an efficiency $\geq 98\%$ even for events with semi-leptonic heavy-flavor quark decays.

To reconstruct photon candidates, projective towers of calorimeter cells with large deposits of energy are used as seeds to create clusters of energy in the EM calorimeter in a cone of radius $\mathcal{R} = 0.4$, where $\mathcal{R} \equiv \sqrt{(\Delta\eta)^2 + (\Delta\phi)^2}$. Once an EM energy cluster is formed, the final energy (E_{EM}) is obtained summing the energies of all the calorimeter cells in a smaller cone of $\mathcal{R} = 0.2$. Photon candidates are required to have: (i) $> 97\%$ of their energy in the EM section; (ii) calorimeter isolation $\mathcal{I} = [E_{\text{tot}}(0.4) - E_{\text{EM}}(0.2)]/E_{\text{EM}}(0.2) < 0.07$, where $E_{\text{tot}}(\mathcal{R})$ [$E_{\text{EM}}(\mathcal{R})$] is the total [EM only] energy in a cone of radius \mathcal{R} ; (iii) scalar sum of p_T less than 1.5 GeV, calculated from all tracks with $p_T > 0.5$ GeV originating

from the $p\bar{p}$ primary interaction point in an annulus of $0.05 < \mathcal{R} < 0.4$ around the EM cluster; and (iv) energy-weighted EM shower width consistent with that expected for an electromagnetic shower. To suppress electrons misidentified as photons, the EM clusters are required to be not spatially matched to significant tracker activity, either a reconstructed track or, in the central rapidity region, a density of hits in the SMT and CFT consistent with that of an electron [17]. In the following, this requirement is referred to as the “track-match veto.”

To further suppress jets misidentified as photons, an artificial neural network (γ -NN) discriminant is defined [8]. It relies on differences between photons and jets in tracker activity, energy deposits in the calorimeter, and in the CPS for the central photons/jets. This γ -NN is trained using PYTHIA [10] Monte Carlo (MC) samples of photon and jet production, which are processed through a GEANT-based [14] simulation of the detector geometry and response. In order to accurately model the effects of multiple $p\bar{p}$ interactions and detector noise, events from random $p\bar{p}$ crossings with a similar instantaneous luminosity spectrum as in data are overlaid on the MC events. These MC events are then processed using the same reconstruction code as for the data. The γ -NN performance is verified using a data sample consisting of photons radiated from leptons in Z boson decays ($Z \rightarrow \ell^+ \ell^- \gamma$, $\ell = e, \mu$) [18]. The γ -NN output O_{NN} distributions for photons in data and MC are in good agreement and exhibit a significant separation from the distribution for misidentified jets [7, 8]. Photon candidates are required to have $O_{\text{NN}} > 0.3$, which is $\approx 98\%$ efficient for photons.

We calculate corrections to the observed number of candidate events to account for the photon detection efficiency and for the acceptance of the selection using simulated samples of $\gamma + b$ -jet events. In these samples, the photon is required to be isolated at particle level by $E_T^{\text{iso}} = E_T^{\text{tot}}(0.4) - E_T^\gamma < 2.5$ GeV, where E_T^{tot} is the total transverse energy of particles within a cone of radius $\mathcal{R} = 0.4$ centered on the photon, and E_T^γ is the photon transverse energy. Here, the particle level includes all stable particles as defined in Ref. [19]. Signal events are generated using the SHERPA [20] and PYTHIA event generators, processed through a GEANT-based [14] simulation and events reconstruction as described above. The acceptance is driven by the selection requirements in η_{det} (applied to avoid edge effects in the calorimeter regions used for the measurement) and ϕ_{det} in the central rapidity region (to avoid periodic calorimeter module boundaries [12] that bias the EM cluster energy and position measurements), photon rapidity y^γ and energy, and bin-to-bin migration effects due to the finite energy and angular resolution of the EM calorimeter. The acceptance varies within (82 – 90)% with a relative systematic uncertainty of (2 – 5)%. The EM clusters reconstructed in the acceptance region are required to pass the photon identification

criteria listed in the previous paragraph. Average correction factors to account for differences between data and simulations are obtained with the SHERPA events, while the difference from the corrections obtained with PYTHIA is used as systematic uncertainty. Small differences between data and MC in the photon selection efficiencies are corrected for with suitable scale factors derived using control samples of electrons from Z boson decays, as well as photons from the radiative Z boson decays [18]. The total efficiency of the above photon selection criteria is (68 – 85)%, depending on the p_T^γ and rapidity region. The systematic uncertainties on these values are 3% for $|y^\gamma| < 1.0$ and 7.3% for $1.5 < |y^\gamma| < 2.5$ and are mainly due to uncertainties caused by the track-match veto, isolation, and the γ -NN requirements. The contamination from $Z(\rightarrow e^+e^-)+\text{jet}$ and $W(\rightarrow e\nu)+\text{jet}$ events is estimated from the simulation and is found to be negligible ($\lesssim 1\%$) for both photon rapidity regions.

At least one jet with $p_T^{\text{jet}} > 15$ GeV and $|y^{\text{jet}}| < 1.5$ must be present in each selected event. Jets are reconstructed using the D0 Run II algorithm [21] with a cone radius of $\mathcal{R} = 0.5$. The jet acceptance with respect to the p_T^{jet} and $|y^{\text{jet}}|$ kinematic cuts varies between 88% and 100% in different photon p_T bins. The uncertainties on the acceptance due to the jet energy scale, jet energy resolution, and difference in energy scale correction between light flavor and b -jets vary between 1% and 7%, increasing for smaller p_T^γ . The jet is required to have at least two associated tracks with $p_T > 0.5$ GeV with at least one hit in the SMT. The track with the highest p_T must have $p_T > 1.0$ GeV. These criteria ensure that there is sufficient information to classify the jet as a heavy-flavor candidate and have a typical efficiency of about 90%. Light jets (caused by light quarks or gluons) are suppressed using a dedicated artificial neural network (b -NN) [9] that employs the longer lifetimes of heavy-flavor hadrons relative to their lighter counterparts. The inputs to the b -NN combine several characteristic quantities of the jet and associated tracks to provide a continuous output value that tends towards one for b -jets and zero for the light jets. The b -NN input variables providing most of the discrimination are the number of reconstructed secondary vertices (SV) in the jet, the invariant mass of charged particle tracks associated with the SV (M_{SV}), the number of tracks used to reconstruct the SV, the two-dimensional decay length significance of the SV in the plane transverse to the beam, a weighted combination of the tracks’ transverse impact parameter significances, and the probability that the tracks associated with the jet originate from the $p\bar{p}$ interaction vertex. The jet is required to have a b -NN output > 0.3 . Depending on p_T^γ , this selection is (40 – 52)% efficient for b -jets with systematic uncertainties of (6 – 23)% for the $\gamma + b$ events with $|y^\gamma| < 1.0$ and of (7 – 11)% for those with $1.5 < |y^\gamma| < 2.5$, both increasing as a function of p_T^γ . Only 0.2 – 0.4% of light jets are misidentified as heavy-

flavor jets, comprising 7% to 10% of the final sample.

After all selection requirements, 199,515 (139,710) events remain in the data samples with the central (forward) photons. In addition to events with light-flavor jets a second source of background is represented by multi-jet events in which one jet is misidentified as a photon. To estimate the photon purity, the γ -NN distribution in data is fitted to a linear combination of templates for photons and jets obtained from simulated $\gamma + \text{jet}$ and dijet samples, respectively. An independent fit is performed in each p_T^γ bin, yielding photon purities between 62% and 99% for the events with the central photons and between 40% and 55% for the events with the forward photons. The obtained photon fractions are shown in Fig. 2. The p_T^γ dependence of the purity is fitted in each region using a two-parameter function $\mathcal{P} = 1 - \exp(a + bp_T^\gamma)$. The systematic uncertainties on the fit are estimated using two alternative fitting functions. These photon purities differ at most by 7% when compared with those obtained for inclusive events, i.e. without the requirement of a heavy-flavor jet. An additional systematic uncertainty in the photon fractions due to the fragmentation model implemented in PYTHIA is also taken into account [22]. This uncertainty is estimated by varying the production rate of π^0 and η mesons by $\pm 50\%$ with respect to their central values [23]. It is found to be about 6% at $p_T^\gamma \simeq 30$ GeV, 2% at $p_T^\gamma \simeq 50$ GeV, and $\leq 1\%$ at $p_T^\gamma \gtrsim 70$ GeV.

The fractions of b -jets are determined by fitting M_{SV} templates for b, c and light jets to the data. Jets from b -quarks tend to have larger values of M_{SV} , in contrast to light jets. For b - and c -jets, the templates are obtained from simulation, while the light jet template is derived from a data sample, enriched in light jets, referred to as negatively tagged data (NT data). The NT data comprises the jets that have negative values for some of the inputs to the b -NN algorithm (such as negative decay length and negative impact parameter significance) which are caused by detector resolution effects [9]. After correcting the NT data for the small contamination from heavy-flavor jets, we have verified that the M_{SV} template shapes in NT data and light jets in the MC simulation agree well.

The result of a maximum likelihood fit to M_{SV} templates, normalized to the number of events in data, is shown in Fig. 3 for central photons with $50 < p_T^\gamma < 60$ GeV, as an example. As shown in Fig. 4, the estimated fraction of b -jets grows with p_T^γ from about 35% to about 42%. The corresponding relative uncertainties range between (4–24)%, increasing at higher p_T^γ and are dominated by the limited data statistics. The data corrected for the photon and jet acceptance, for reconstruction efficiencies, for the contribution of background events, and for bin-migration effects, are presented at the particle level, as defined in Ref. [19].

The differential cross sections of $\gamma + b$ production are extracted in nine (six) bins of p_T^γ for central (forward)

photons, and are listed in Tables I and II. The results are also shown in Fig. 5 as a function of p_T^γ for the two photon rapidity intervals. The data points are plotted at the value of p_T^γ for which the value of the smooth function describing the cross section equals the averaged cross section in the bin [24]. The $\gamma + b$ -jet simulated sample with Sherpa has been used to determine mean p_T^γ values.

The cross sections with the central (forward) photons fall by about four (three) orders of magnitude in the range $30 < p_T^\gamma < 300$ (200) GeV. The statistical uncertainty on the results ranges from 2% in the first p_T^γ bin to $\approx 11\%$ in the last p_T^γ bins, while the total systematic uncertainty varies between 12% and 36%. The main source of the uncertainty at low p_T^γ is due to the photon purity (up to 8%), the b -jet fraction fit (6–7%), and the luminosity (6.1%) [15]. At higher p_T^γ , the uncertainty is dominated by the fractions of b -jets and their selection efficiencies. Systematic uncertainties are highly bin-to-bin correlated for the first three p_T^γ bins, while the total systematic uncertainty is nearly uncorrelated across the bins at $p_T^\gamma > 70$ GeV.

Next-to-leading order (NLO) perturbative QCD predictions, with the renormalization scale μ_R , factorization scale μ_F , and fragmentation scale μ_f all set to p_T^γ , are also given in Tables I and II. These predictions [1] are based on a phase space slicing method used to calculate the cross section analytically [25]. The uncertainty from the choice of scale is estimated through a simultaneous variation of all three scales by a factor of two, i.e. for $\mu_{R,F,f} = 0.5p_T^\gamma$ and $2p_T^\gamma$. The predictions utilize CTEQ6.6M PDFs [11] and are corrected for non-perturbative effects of parton-to-hadron fragmentation and multiple parton interactions. The latter are evaluated using SHERPA and PYTHIA MC samples using their default settings [10, 20]. The overall correction varies from about 0.90 at $30 < p_T^\gamma < 40$ GeV to about 0.95 at high p_T^γ , and an uncertainty of $\lesssim 2\%$ is assigned to account for the difference between the two MC generators.

The prediction based on the k_T -factorization approach [26, 27] and unintegrated parton distributions [28] are also given in Tables I and II. The k_T -factorization formalism contains additional contributions to the cross sections due to resummation of gluon radiation diagrams with k_T^2 above a scale μ^2 , $O(1 \text{ GeV})$, where k_T denotes the transverse momentum of the radiated gluon. Apart from this resummation, the non-vanishing transverse momentum distribution of the colliding partons are taken into account. These effects lead to a broadening of the photon transverse momentum distribution in this approach [26]. The scale uncertainties on these predictions vary from about 31% (–28%) at $30 < p_T^\gamma < 40$ GeV to about 5% (14%) for the central photons and 26% (–13%) for the forward photons in the last p_T^γ bin.

Tables I and II also contain predictions of the PYTHIA [10] MC event generator with the CTEQ6.1L PDF set. It

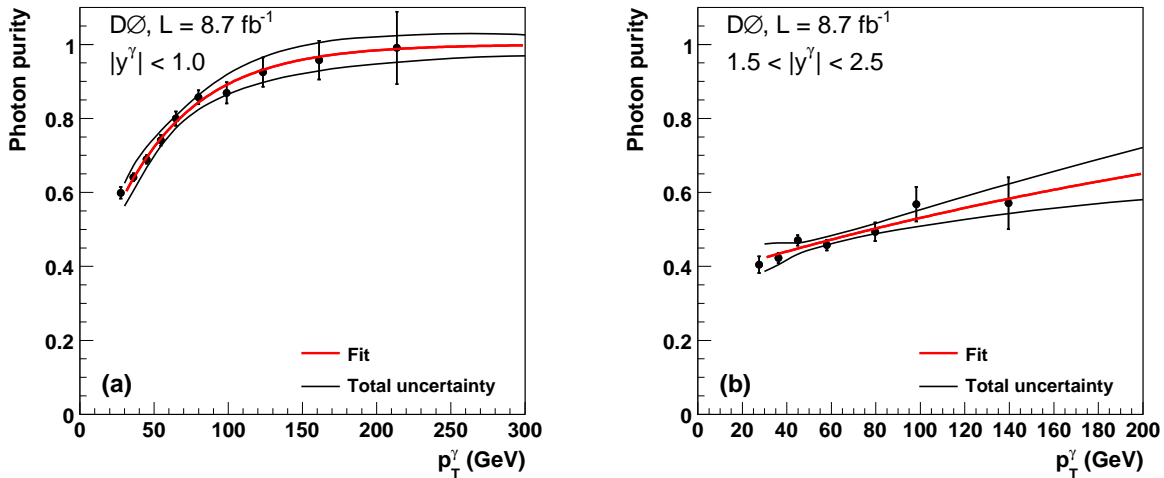


FIG. 2: Photon purity as a function of p_T^γ in the selected data sample in the central rapidity region $|y^\gamma| < 1.0$ (a) and the forward rapidity region $1.5 < |y^\gamma| < 2.5$ (b).

includes only $2 \rightarrow 2$ matrix elements (ME) with $gb \rightarrow \gamma b$ and $q\bar{q} \rightarrow \gamma g$ scatterings (defined at LO) and, with $g \rightarrow b\bar{b}$ splitting in the parton shower (PS). We also provide predictions by the SHERPA MC event generator [20] with the CTEQ6.6M PDF set [11]. For $\gamma + b$ production, SHERPA includes all the MEs with one photon and up to three jets, with at least one b -jet in our kinematic region. In particular, it accounts for an additional hard jet that accompanies the photon associated with a $b\bar{b}$ pair. Compared to an NLO calculation, there is an additional benefit of imposing resummation (further emissions) through the consistent combination with the PS. Matching between the ME partons and the PS jets follows the prescription given in Ref. [29]. Systematic uncertainties are estimated by varying the ME-PS matching scale by ± 5 GeV around the chosen central value [30]. As a result, the SHERPA cross sections vary up to $\pm 7\%$ for the central photons and up to $-25\%/+17\%$ for the forward photons, where the uncertainty is largest in the first p_T^γ bin.

All the theoretical predictions are obtained including the isolation requirement on the photons $E_T^{\text{iso}} < 2.5$ GeV at the particle level. The predictions are compared to data in Fig. 5 as a function of p_T^γ . The ratios of data over the NLO QCD calculations and of different QCD predictions or MC simulation to the same NLO QCD calculations are shown in Fig. 6 as a function of p_T^γ for both central and forward photons. The ratio of NLO predictions with CTEQ6.6M to those with MSTW2008 [31] and ABKM09NLO [32] are also shown on the plots.

The measured cross sections are in agreement with the NLO QCD predictions within theoretical and experimental uncertainties in the region up to $p_T^\gamma \lesssim 70$ GeV, but show notable disagreement for larger p_T^γ . The cross sec-

tion slopes in data significantly differ from the predicted ones in both photon rapidity regions. The results indicate a need for higher order perturbative QCD corrections in the large p_T^γ region, that is dominated by the annihilation process $q\bar{q} \rightarrow \gamma g$ ($g \rightarrow b\bar{b}$), and resummation of diagrams with additional gluon radiation. The QCD predictions from the k_T -factorization approach is in better agreement with data. The best agreement is obtained with the SHERPA MC that allows up to two extra hard partons (jets) in ME in addition to the b -quark (jet) and includes the consistent treatment of the possible contributions from the parton shower. However, correcting the SHERPA predictions by including additional higher order contributions, as is done, for instance, for W +jets events, would be desirable [33].

In conclusion, we have performed a measurement of the differential cross section of inclusive production of photon in association with b -jets at the Tevatron $p\bar{p}$ collider. The results cover the kinematic ranges $30 < p_T^\gamma < 300$ GeV with $|y^\gamma| < 1.0$, and $30 < p_T^\gamma < 200$ GeV with $1.5 < |y^\gamma| < 2.5$. A good description of the data can only be achieved by including higher order corrections into the NLO QCD predictions, which are currently present as additional real emissions in the SHERPA MC generator. These results can be used to improve the description of background processes in searches for the Higgs boson or for new phenomena beyond the SM at the Tevatron and the LHC in final states involving the production of vector bosons in association with b -jets.

We are grateful to the authors of the theoretical calculations, T. Stavreva, J. Owens, N. Zotov, S. Schumann and F. Siegert, for providing predictions and for many useful discussions.

We thank the staffs at Fermilab and collaborating institutions, and acknowledge support from the DOE

TABLE I: The $\gamma + b$ production cross section $d\sigma/dp_T^\gamma$ in bins of p_T^γ for $|y^\gamma| < 1.0$ together with statistical, $\delta\sigma_{\text{stat}}$, and systematic, $\delta\sigma_{\text{syst}}$, uncertainties. The last four columns show theoretical predictions obtained within NLO QCD, k_T factorization, PYTHIA and SHERPA event generators.

p_T^γ bin (GeV)	$\langle p_T^\gamma \rangle$ (GeV)	$d\sigma/dp_T^\gamma$ (pb/GeV)							
		Data	$\delta_{\text{stat}}(\%)$	$\delta_{\text{syst}}(\%)$	$\delta_{\text{tot}}(\%)$	NLO	k_T fact.	PYTHIA	SHERPA
30 – 40	34.2	1.59×10^0	2	12	12	1.80×10^0	1.60×10^0	1.24×10^0	1.62×10^0
40 – 50	44.3	6.30×10^{-1}	3	11	11	5.60×10^{-1}	5.47×10^{-1}	4.23×10^{-1}	6.38×10^{-1}
50 – 60	54.3	2.85×10^{-1}	3	11	11	2.14×10^{-1}	2.25×10^{-1}	1.63×10^{-1}	2.63×10^{-1}
60 – 70	64.5	1.42×10^{-1}	4	10	11	9.49×10^{-2}	1.05×10^{-1}	7.27×10^{-2}	1.25×10^{-1}
70 – 90	78.1	5.77×10^{-2}	4	11	11	3.64×10^{-2}	4.32×10^{-2}	2.88×10^{-2}	5.20×10^{-2}
90 – 110	98.6	2.14×10^{-2}	6	14	15	1.19×10^{-2}	1.59×10^{-2}	1.00×10^{-2}	1.82×10^{-2}
110 – 140	122.0	7.85×10^{-3}	9	18	20	4.08×10^{-3}	6.06×10^{-3}	3.76×10^{-3}	6.63×10^{-3}
140 – 180	156.4	2.31×10^{-3}	7	24	25	1.18×10^{-3}	2.02×10^{-3}	1.19×10^{-3}	1.99×10^{-3}
180 – 300	215.8	3.60×10^{-4}	11	36	38	1.61×10^{-4}	3.55×10^{-4}	1.91×10^{-4}	2.90×10^{-4}

TABLE II: The $\gamma + b$ production cross section $d\sigma/dp_T^\gamma$ in bins of p_T^γ for $1.5 < |y^\gamma| < 2.5$ together with statistical, $\delta\sigma_{\text{stat}}$, and systematic, $\delta\sigma_{\text{syst}}$, uncertainties. The last four columns show theoretical predictions obtained within NLO QCD, k_T factorization, PYTHIA and SHERPA event generators.

p_T^γ bin (GeV)	$\langle p_T^\gamma \rangle$ (GeV)	$d\sigma/dp_T^\gamma$ (pb/GeV)							
		Data	$\delta_{\text{stat}}(\%)$	$\delta_{\text{syst}}(\%)$	$\delta_{\text{tot}}(\%)$	NLO	k_T fact.	PYTHIA	SHERPA
30 – 40	34.2	9.05×10^{-1}	2	16	16	9.68×10^{-1}	1.04×10^0	4.51×10^{-1}	7.95×10^{-1}
40 – 50	44.2	2.79×10^{-1}	3	15	15	2.74×10^{-1}	3.38×10^{-1}	1.55×10^{-1}	2.91×10^{-1}
50 – 70	57.4	8.30×10^{-2}	4	14	14	6.47×10^{-2}	8.34×10^{-2}	4.08×10^{-2}	8.06×10^{-2}
70 – 90	77.7	1.79×10^{-2}	6	16	17	1.11×10^{-2}	1.74×10^{-2}	8.26×10^{-3}	1.59×10^{-2}
90 – 110	97.8	4.38×10^{-3}	10	19	22	2.50×10^{-3}	4.75×10^{-3}	2.18×10^{-3}	3.95×10^{-3}
110 – 200	124.9	4.65×10^{-4}	11	29	31	2.12×10^{-4}	5.02×10^{-4}	2.06×10^{-4}	3.70×10^{-4}

and NSF (USA); CEA and CNRS/IN2P3 (France); MON, Rosatom and RFBR (Russia); CNPq, FAPERJ, FAPESP and FUNDUNESP (Brazil); DAE and DST (India); Colciencias (Colombia); CONACyT (Mexico); NRF (Korea); FOM (The Netherlands); STFC and the Royal Society (United Kingdom); MSMT and GACR (Czech Republic); BMBF and DFG (Germany); SFI (Ireland); The Swedish Research Council (Sweden); and CAS and CNSF (China).

- [7] V.M. Abazov *et al.* (D0 Collaboration), Phys. Lett. B **690**, 108 (2010).
- [8] V.M. Abazov *et al.* (D0 Collaboration), Phys. Rev. Lett. **102**, 231801 (2009).
- [9] V.M. Abazov *et al.* (D0 Collaboration), Nucl. Instrum. Methods in Phys. Res. A **620**, 490 (2010).
- [10] T. Sjöstrand, S. Mrenna, and P.Z. Skands, J. High Energy Phys. **05**, 026 (2006). We use PYTHIA version v6.420 with tune A.
- [11] W.K. Tung *et al.*, J. High Energy Phys. **02**, 052 (2007).
- [12] V.M. Abazov *et al.* (D0 Collaboration), Nucl. Instrum. Methods in Phys. Res. A **565**, 463 (2006); R. Angstadt *et al.*, Nucl. Instrum. Methods Phys. Res. A **622**, 298 (2010). M. Abolins *et al.*, Nucl. Instrum. Methods in Phys. Res. A **584**, 75 (2008);
- [13] The polar angle θ and the azimuthal angle ϕ are defined with respect to the positive z axis, which is along the proton beam direction. Pseudorapidity is defined as $\eta = -\ln[\tan(\theta/2)]$. Also, η_{det} and ϕ_{det} are the pseudorapidity and the azimuthal angle measured with respect to the center of the detector.
- [14] R. Brun and F. Carminati, CERN Program Library Long Writeup, W5013, (1993); we use GEANT version v3.21.
- [15] T. Andeen *et al.*, FERMILAB-TM-2365 (2007).
- [16] The primary $p\bar{p}$ interaction vertex is that found to be the most likely collision point, among possibly several collisions within a specific beam crossing, from which our selected objects emanate. The algorithm for defining it can be found in [9].
- [17] V.M. Abazov *et al.* (D0 Collaboration), Phys. Lett. B **659**, 856 (2008).
- [18] V.M. Abazov *et al.* (D0 Collaboration), Phys. Rev. D **85**,

- [1] T. Stavreva and J.F. Owens, Phys. Rev. D **79**, 054017 (2009).
- [2] V.M. Abazov *et al.* (D0 Collaboration), Phys. Rev. Lett. **94**, 161801 (2005). T. Aaltonen *et al.* (CDF Collaboration), Phys. Rev. D **74**, 032008 (2006).
- [3] T. Aaltonen *et al.* (CDF Collaboration), Phys. Rev. D **79**, 052008 (2009).
- [4] V.M. Abazov *et al.* (D0 Collaboration), Phys. Rev. D **83**, 031105 (2011).
- [5] T. Aaltonen *et al.* (CDF Collaboration), Phys. Rev. D **81**, 052006 (2010).
- [6] V.M. Abazov *et al.* (D0 Collaboration), Phys. Rev. Lett. **102**, 192002 (2009).

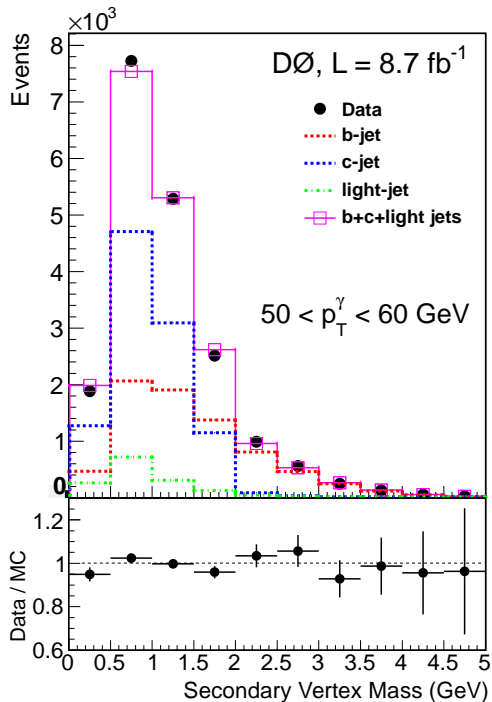


FIG. 3: Distribution of observed events for secondary vertex mass after all selection criteria for the representative bin $50 < p_T^\gamma < 60$ GeV ($|y^\gamma| < 1.0$). The distributions for the b -, c -, and light jet templates are shown normalized to their respective fitted fractions. Also included at the bottom is the ratio of data to the result of the fit. Fits in the other p_T^γ bins are of similar quality.

052001 (2012).

- [19] C. Buttar *et al.*, arXiv:0803.0678 [hep-ph], section 9.
- [20] T. Gleisberg *et al.*, J. High Energy Phys. **02**, 007 (2009). We use SHERPA version v1.3.1.
- [21] G.C. Blazey *et al.*, arXiv:hep-ex/0005012 (2000).
- [22] V.M. Abazov *et al.* (D0 Collaboration), Phys. Lett. B **639**, 151 (2006).
- [23] T. Binoth *et al.*, Eur. Phys. J. C **4**, 7 (2002).
- [24] G.D. Lafferty and T.R. Wyatt, Nucl. Instrum. Methods in Phys. Res. A **355**, 541 (1995).
- [25] B.W. Harris and J. Owens, Phys. Rev. D **65**, 094032 (2002).
- [26] A.V. Lipatov and N.P. Zotov, J. Phys. G **34**, 219 (2007); S.P. Baranov, A.V. Lipatov, and N.P. Zotov, Eur. Phys. J. C **56**, 371 (2008).
- [27] A.V. Lipatov and N.P. Zotov, paper in preparation.
- [28] M.A. Kimber, A.D. Martin, and M.G. Ryskin, Phys. Rev. D **63** 114027 (2001).
- [29] A. D. Martin, W. J. Stirling, R. S. Thorne, and G. Watt, Eur. Phys. J. C **63**, 189 (2009).
- [30] We choose the following ME-PS matching parameters: the energy scale $Q_0 = 15$ GeV and the spatial scale $D = 0.4$, where D is taken to be of the size of the photon isolation cone.
- [31] A. D. Martin, W. J. Stirling, R. S. Thorne, and G. Watt, Eur. Phys. J. C **63**, 189 (2009).
- [32] S. Alekhin *et al.*, Phys. Rev. D **81**, 014032 (2010).
- [33] C. F. Berger *et al.*, arXiv:0905.2735 [hep-ph].

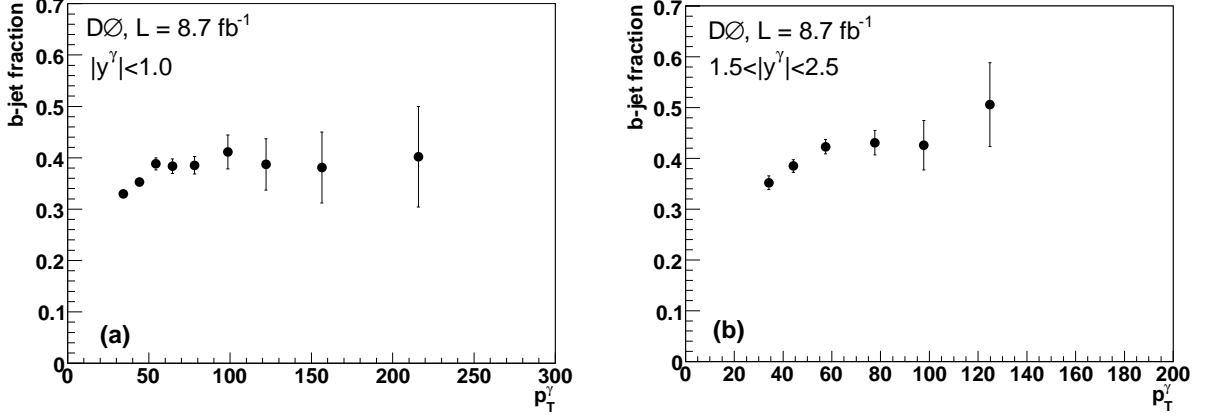


FIG. 4: The b -jet fraction (with total uncertainties) as a function of p_T^γ in the data sample after applying all selections in the central rapidity region $|y^\gamma| < 1.0$ (a) and the forward rapidity region $1.5 < |y^\gamma| < 2.5$ (b).

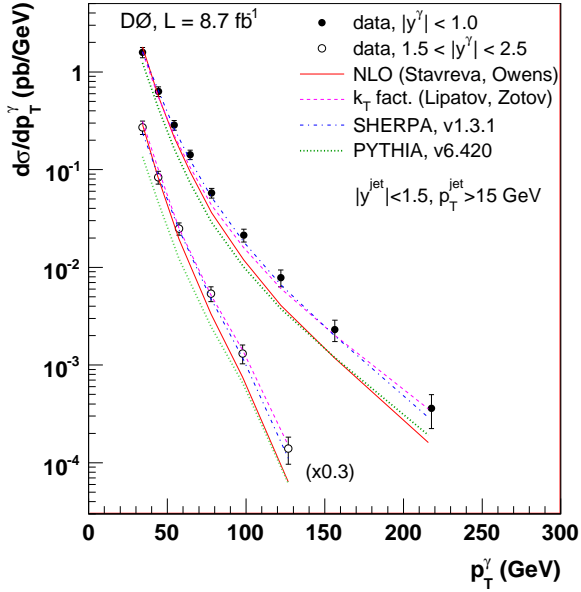


FIG. 5: The $\gamma + b$ production differential cross sections as a function of p_T^γ in the two photon rapidity regions, $|y^\gamma| < 1.0$ and $1.5 < |y^\gamma| < 2.5$ (the latter results are multiplied by 0.3 for presentation). The uncertainties on the data points include statistical and systematic contributions added in quadrature. The measurements are compared to the NLO QCD calculations using CTEQ6.6M PDFs [11] (solid line). The predictions from SHERPA, PYTHIA and “ k_T factorization” approach [26, 27] are shown by the dash-dotted, dotted and dashed lines, respectively.

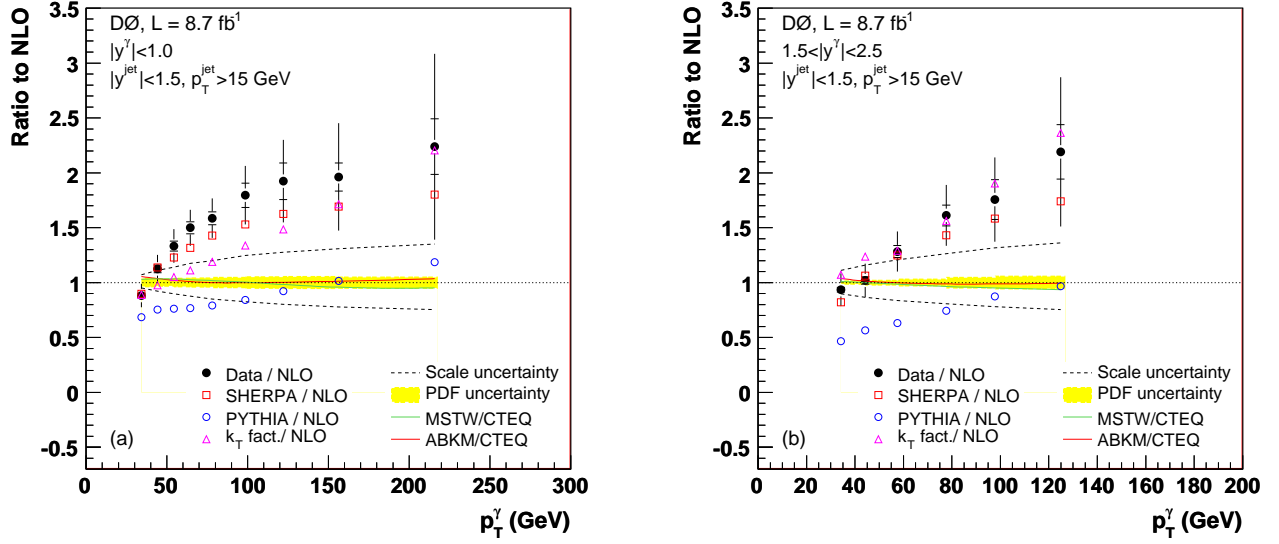


FIG. 6: The ratio of $\gamma + b$ production differential cross sections between data and NLO QCD predictions with uncertainties for the rapidity regions $|y^\gamma| < 1.0$ (a) and $1.5 < |y^\gamma| < 2.5$ (b). The uncertainties on the data include both statistical (inner error bar) and full uncertainties (entire error bar). Also shown are the uncertainties on the theoretical QCD scales and the CTEQ6.6M PDFs. The ratio of NLO predictions with CTEQ6.6M to those with MSTW2008 [31] and ABKM09NLO [32] are also shown.